Performance Analysis of Roll-Invariant PolSAR Parameters from C-band images with Regard to Sea Ice Type Separation

Debanshu Ratha[a], A. Malin Johansson[a], Andrea Marinoni[a,b], and Torbjørn Eltoft[a]
[a]UiT The Arctic University of Norway, Tromsø, Norway
[b]University of Cambridge, Cambridge, United Kingdom

Abstract

The Polarimetric Synthetic Aperture Radar (PolSAR) backscatter from a target is dependent on the incidence angle. Consequently, the associated roll invariant parameters are affected by changes in incidence angle. In this work, we identify a few of these parameters that remain robust in identifying sea ice features even under large incidence angle variations. We conclude that the *helicity angle* and the *degree of purity* are preferable over the *scattering type angle* in this respect. We utilize two overlapping RADARSAT-2 C-Band full polarimetric images, with a time difference of less than 2 hours, but with significant incidence angle difference.

1 Introduction

The Arctic ocean ice is undergoing significant changes, with a reduced sea ice cover and a higher degree of First Year ice (FYI). Discrimination between different sea ice types is important both for operational sea ice mapping as well as to enable estimates of changes in sea ice types. For operational sea ice mapping dual-polarimetric SAR images is preferable due to their larger areal coverage, besides the European Space Agency (ESA) Sentinel-1 satellites offer near daily coverage over the Arctic Ocean. Fully polarimetric images enable high resolution parameter retrieval, and can be used to retrieve information about sea ice scattering mechanisms, e.g, [6, 14, 4], but they typically have small areal swaths. Within this study, we use fully polarimetric RADARSAT-2 images to investigate separability between different sea-ice types using a recently proposed novel set of roll-invariant polarimetric parameters derived using a geodesic distance [11]. We aim to separate three different sea ice types: young ice, level sea ice and deformed sea ice from the C-Band images.

Several previous studies have explored the feasibility of polarimetric parameters for sea ice classification, some using the H/A/α decomposition, e.g., [12] and [14]. Using X-band stripmap images [12] studied the usefulness of 12 different polarimetric parameters for discriminating between open water, young ice, smooth FYI, rough and deformed FYI and multi-year ice (MYI) and found the H/A/α to rank among the top 6 parameters. Moreover, [3] observed lower scattering entropy values for the young ice and rafted thin ice compared to the surrounding thicker sea ice. In a recent paper [8], even reducing fully polarimetric images to include only the two co-polarized bands, the entropy parameter was still comparably useful for separation of thin ice from the other thicker sea ice types.

2 Statement of Objectives

In [11], the authors introduced a set of roll invariant PolSAR parameters, which are defined through the geodesic distances to certain elementary targets and the *ideal depolarizer*. The parameters are denoted as α_{GD}, τ_{GD} and P_{GD}, and defined in the next section. The objectives of this work are:

1. To investigate if these parameters can separate between different sea-ice classes.
2. To identify which of the parameters has the best discrimination power.
3. To determine which parameters among these are most robust under large incidence angle changes.

3 Theory

A PolSAR observation in the linear HV-basis (i.e., horizontal and vertical polarizations) consists of a 2×2 complex matrix known as the scattering matrix $\mathbf{S}$. The $\mathbf{S}$ captures the backscatter in the channels characterized by one transmit and other received polarization.

$$\mathbf{S} = \begin{bmatrix} S_{HH} & S_{VH} \\ S_{HV} & S_{VV} \end{bmatrix} \tag{1}$$

Under monostatic conditions, the reciprocity theorem yields $S_{HV} = S_{VH}$ making $\mathbf{S}$ symmetric.

The $\mathbf{S}$ can also be encoded as a target vector using the lexicographic or Pauli basis. The respective target vectors $\vec{k}_L$ and $\vec{k}_P$ can be utilized to arrive at second order statistics of backscatter measurements by computing the covariance ($\mathbf{C}$) or coherency matrix ($\mathbf{T}$) respectively. The Kennaugh matrix on the other hand is also a second order representation of the backscatter information as a 4×4 real matrix.

It is important to recall here that the 4×4 Kennaugh matrix is the power representation of the PolSAR backscatter information under the Stokes formalism [7]. Thus, it is equivalent to working with 3×3 complex (Hermitian) covariance ($\mathbf{C}$) equivalently coherency ($\mathbf{T}$) matrix. A one-to-one correspondence exists between the complex and the real form of PolSAR backscatter information.
The relationship between a coherency matrix $\mathbf{T}$ and its $\mathbf{K}$ form is given below [1]:

$$\mathbf{K} = \begin{bmatrix} \frac{T_{11}+T_{22}+T_{33}}{2} & \Re(T_{12}) & \Re(T_{13}) & \Im(T_{23}) \\ \Re(T_{12}) & \frac{T_{11}+T_{22}-T_{33}}{2} & \Re(T_{23}) & \Im(T_{13}) \\ \Re(T_{13}) & \Re(T_{23}) & \frac{T_{11}-T_{22}+T_{33}}{2} & -\Im(T_{12}) \\ \Im(T_{23}) & \Im(T_{13}) & -\Im(T_{12}) & \frac{-T_{11}+T_{22}+T_{33}}{2} \end{bmatrix} \tag{2}$$

where $\Re(\cdot)$ and $\Im(\cdot)$ denote real and imaginary parts of a complex number and T_{ij} denotes the (i,j)-th entry of $\mathbf{T}$.
To obtain the Kennaugh matrix $\mathbf{K}$ from the coherent PolSAR scattering matrix $\mathbf{S}$ the following expression is used [1]:

$$\mathbf{K} = \frac{1}{2}\mathbf{A}^*(\mathbf{S} \otimes \mathbf{S}^*)\mathbf{A}^{*T}, \quad \mathbf{A} = \begin{bmatrix} 1 & 0 & 0 & 1 \\ 1 & 0 & 0 & -1 \\ 0 & 1 & 1 & 0 \\ 0 & j & -j & 0 \end{bmatrix}, \tag{3}$$

where $\otimes$ is the Kronecker product, superscripts $\cdot^*$ and $\cdot^T$ denote conjugate and transpose, respectively, and $j = \sqrt{-1}$. The transpose operator is always used in the superscript, and not be confused with the coherency matrix.
For any two Kennaugh matrices $\mathbf{K}_1$ and $\mathbf{K}_2$ the geodesic distance between them is defined as [10]:

$$GD(\mathbf{K_1}, \mathbf{K_2}) = \frac{2}{\pi}\cos^{-1}\left(\frac{Tr(\mathbf{K_1}^T\mathbf{K_2})}{\sqrt{Tr(\mathbf{K_1}^T\mathbf{K_1})}\sqrt{Tr(\mathbf{K_2}^T\mathbf{K_2})}}\right) \tag{4}$$

where Tr is the trace operator.
The geodesic distance was first utilized with reference PolSAR scatterers [10] for change detection. In subsequent works, the approach has been found to be successful in catering to a number of applications e.g. vegetation monitoring, built-up mapping and land-use/land-cover classification. In [11], three new roll invariant parameters were proposed which utilized the trihedral corner reflector (t), left (lh) and right helices (rh), and the ideal depolarizer (dep) as reference scatterers. These parameters correspond to scattering type (α_{GD}), helicity (τ_{GD}), and degree of purity (P_{GD}) for an observed PolSAR pixel. The α_{GD} and P_{GD} have counterparts in literature i.e., Cloude-α [2], and P_D [5]. However, in computing these parameters the eigenvalue decomposition as in case of α was no more necessary. The third parameter τ_{GD} which was compared with helicity parameter τ_{m_1} [13], was found to be of different nature. In the end, the τ_{GD} parameter was interpreted as a measure of asymmetry through its corresponding reference target helix which is an asymmetric scatterer. Thus, the above parameters were a means to describe the target using the geodesic distance (GD) and reference canonical targets in a much simpler form.
The equations (5)–(8) provide the Kennaugh matrix forms for trihedral, left and right helices, and the ideal depolarizer. These reference scatterers are utilized to define the three GD-based roll invariant PolSAR parameters.

$$\mathbf{K}_t = \begin{bmatrix} 1 & 0 & 0 & 0 \\ 0 & 1 & 0 & 0 \\ 0 & 0 & 1 & 0 \\ 0 & 0 & 0 & -1 \end{bmatrix} \tag{5}$$

$$\mathbf{K}_{lh} = \begin{bmatrix} 1 & 0 & 0 & -1 \\ 0 & 0 & 0 & 0 \\ 0 & 0 & 0 & 0 \\ -1 & 0 & 0 & 1 \end{bmatrix} \tag{6}$$

$$\mathbf{K}_{rh} = \begin{bmatrix} 1 & 0 & 0 & 1 \\ 0 & 0 & 0 & 0 \\ 0 & 0 & 0 & 0 \\ 1 & 0 & 0 & 1 \end{bmatrix} \tag{7}$$

$$\mathbf{K}_{dep} = \begin{bmatrix} 1 & 0 & 0 & 0 \\ 0 & 0 & 0 & 0 \\ 0 & 0 & 0 & 0 \\ 0 & 0 & 0 & 0 \end{bmatrix} \tag{8}$$

Equations (9)–(11) define the the three roll-invariant parameters namely α_{GD}, τ_{GD} and P_{GD} respectively for an observed Kennaugh matrix $\mathbf{K}$.

$$\alpha_{GD} = 90^\circ \times GD(\mathbf{K}, \mathbf{K}_t) \tag{9}$$

$$\tau_{GD} = 45^\circ \times (1 - \sqrt{GD(\mathbf{K}, \mathbf{K}_{lh}) \times GD(\mathbf{K}, \mathbf{K}_{rh})}) \tag{10}$$

$$P_{GD} = \left(\frac{3}{2} \times GD(\mathbf{K}, \mathbf{K}_{dep})\right)^2 \tag{11}$$

4 Satellite data and study area

The fully polarimetric RADARSAT-2 images used here were collected to overlap with one of the Nansen Legacy campaigns (https://arvenetternansen.com) in December 2019 north of Svalbard, for image specifics see Table 1. The temperature observation at the time of the image acquisitions was -14 °C and the wind speeds approximately 7 m/s, for more information see [9]. Within the images used here level and deformed older sea ice as well as young ice is observed. Additionally, a multi-looking of 10×10 has been applied on these data sets before computing the PolSAR parameters.

Table 1 Specifics of RADARSAT-2 satellite data used in this study. The images cover 25x25 km with a range (rg) and azimuth (az) resolution of 5.2 m (rg) x 7.6 m (az). Both are ascending passes with large incidence angle (IA) difference.

Name	Date	Time (UTC)	IA (°)
R1	02.12.19	12:43	19.7–21.6
R2	02.12.19	14:23	39.3–40.7

5 Preliminary Results and Analysis

Figure 1 and Figure 2 provide the Pauli RGB image and the parameter maps corresponding to α_{GD}, τ_{GD} and P_{GD} for the two RADARSAT-2 images, respectively. For a direct comparison between the two images the colour bars are set to the common minimum and maximum values in case of the parameter maps.

Within the Pauli RGB images shown in Figure 1 and 2 some leads with young ice is seen extending from the top left towards the bottom right of the images. They are observed as purple. Deformed sea ice is observable as the whiter areas in the Pauli RGB images, and are seen, e.g., in the central parts of the images. At the top and at the lower left corner of both these images we can observe some the darker patches, corresponding to areas of level ice.

Comparing the results for the two RADARSAT-2 images R1 and R2, we observe that the leads with young ice in both images have lower τ_{GD} and higher P_{GD} than the surrounding thicker sea ice. The α_{GD} values in R1 are between $10°$ and $15°$, above average, the τ_{GD} values are between $0°$ and $2°$, which are below average, and the P_{GD} values are between 0.9 and 1, which are above the average.

For R2, the P_{GD} values are >0.85, clearly separating the lead from the surrounding sea ice areas. The τ_{GD} values are between $0°$ and $2°$, which are below the average. The α_{GD} values of the leads are also in this image, ranging between $10°$ and $15°$. The separation from the its surrounding ice is less distinct.

The deformed sea ice, observable as the whiter areas in the Pauli RGB images, has similar α_{GD} values as the leads in R1, whereas both the τ_{GD} and P_{GD} values are lower, typically in the ranges of $4°$ and 0.75, respectively. For R2 the τ_{GD} values for the deformed sea ice areas are higher than for the surrounding less deformed and younger sea ice, with values between $6°$ and $8°$, The P_{GD} values are between 0.6 and 0.75. As stated above, the α_{GD} is similar to the Cloude-α [2] that in [12] was found to be suitable to separate particularly young ice from surrounding thicker sea ice. This is also observable in this study.

The level sea ice has low α_{GD} values in R1, ranging between $0°$ and 5, low τ_{GD} values and medium high P_{GD}. The values for the latter two are located between the deformed and the young ice values. In R2, the smooth ice areas are easier to separate from the surrounding sea ice. Here the α_{GD} values are lower than for the other sea ice types, with values between $5°$ and $10°$. The τ_{GD} values are higher than for the young ice and lower than for the deformed sea ice, with values between $2°$ and $4°$. Finally, for level ice the P_{GD} values are lower than for the young ice, but higher than for the deformed sea ice. The values are here between 0.8 and 0.9.

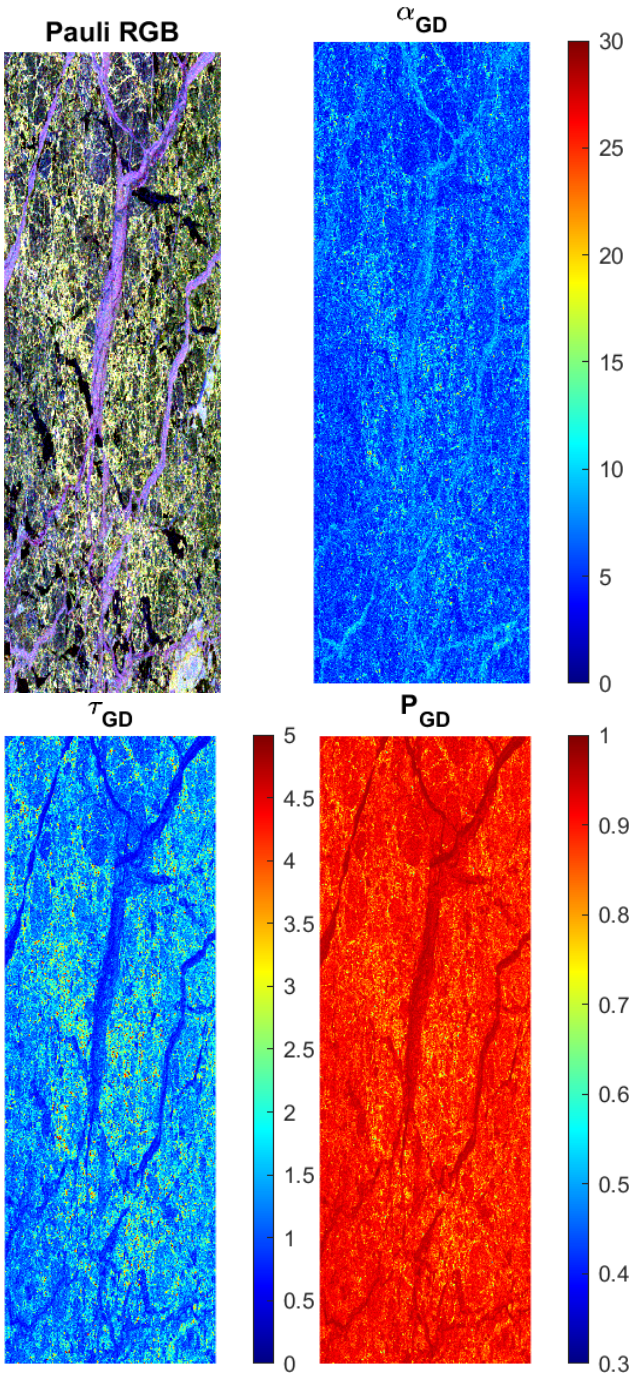

Figure 1 Pauli RGB image and roll invariant PolSAR parameters computed shown for image R1.

6 Conclusion

We observe that the helicity angle (τ_{GD}), and the degree of purity (P_{GD}) can be used to separate three different sea ice types within fully polarimetric RADARSAT-2 images. These two features seem to have stronger discrimination power than the scattering type angle (α_{GD}). In fact, this is encouraging, taking into account the large difference in incidence angle, i.e. ($20°$), of the two satellite images used within the study.

7 Acknowledgement

RADARSAT-2 data was provided by NSC/KSAT under the Norwegian-Canadian RADARSAT agreement 2019. Observations were provided by the Research Council of Norway (RCN) Nansen Legacy project (RCN project 276730). The authors are grateful to all those who participated in the

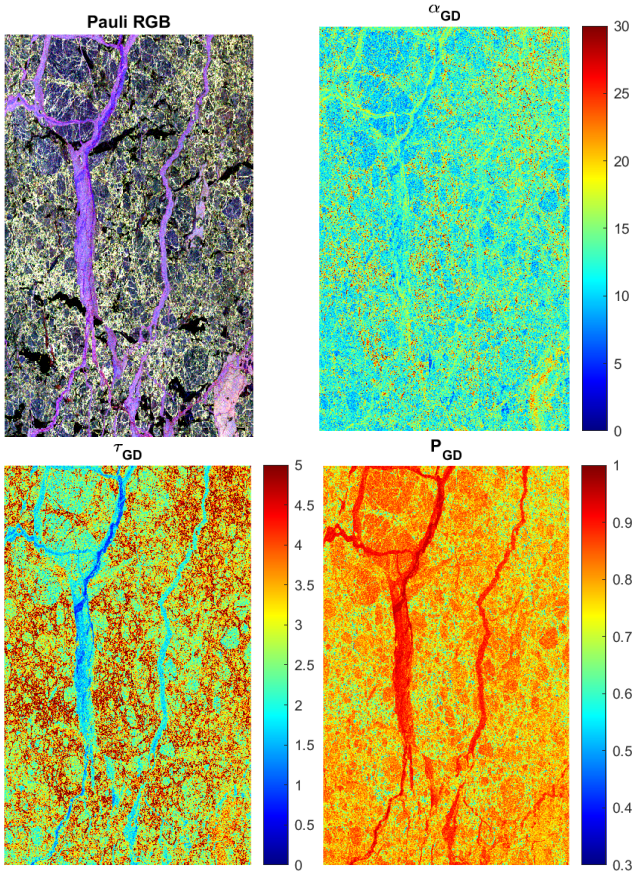

Figure 2 Pauli RGB image and roll invariant PolSAR parameters computed shown for image R2.

fieldwork experiments. This work was supported in part by RCN through the "Centre for Integrated Remote Sensing and Forecasting for Arctic Operations" (CIRFA) (RCN project 237906), and the European Union's Horizon 2020 research and innovation programme under grant agreement No. 825258.

8 Literature

[1] Cloude, S. (2010). *Polarisation: applications in remote sensing*. Oxford University Press.

[2] Cloude, S. R. and Pottier, E. (1997). An entropy based classification scheme for land applications of polarimetric SAR. *IEEE Trans. Geosci. Remote Sens.*, 35(1):68–78.

[3] Dierking, W. and Wesche, C. (2014). C-band radar polarimetry useful for detection of icebergs in sea ice? *IEEE Trans. Geosci. Remote Sens.*, 52(1):25–37.

[4] Geldsetzer, T., Arkett, M., Zagon, T., Charbonneau, F., Yackel, J., and Scharien, R. (2015). All-season compact-polarimetry c-band sar observations of sea ice. *Can. J. Remote. Sens.*, 41(5):485–504.

[5] Gil, J. J. and Bernabeu, E. (1985). A depolarization criterion in Mueller matrices. *Optica Acta: International Journal of Optics*, 32(3):259–261.

[6] Gill, J., Yackel, J., and Geldsetzer, T. (2013). Analysis of consistency in first-year sea ice classification potential of c-band sar polarimetric parameters. *Can. J. Remote. Sens.*, 39(2):101–117.

[7] Huynen, J. R. (1970). *Phenomenological theory of radar targets*. PhD thesis, Technical Univ., Delft, The Netherlands.

[8] Johansson, A. M., Brekke, C., Spreen, G., and A., K. J. (2018). X-, c-, and l-band sar signatures of newly formed sea ice in arctic leads during winter and spring. *Remote Sens. Environ.*, 204:162–180.

[9] Johansson, A. M., Espeseth, M. M., Brekke, C., and Holt, B. (2020). Can mineral oil slicks be distinguished from newly formed sea ice using synthetic aperture radar? *IEEE Journal of Selected Topics in Applied Earth Observations and Remote Sensing*, 13:4996–5010.

[10] Ratha, D., De, S., Celik, T., and Bhattacharya, A. (2017). Change detection in polarimetric SAR images using a geodesic distance between scattering mechanisms. *IEEE Geosci. Remote Sens. Lett.*, 14(7):1066–1070.

[11] Ratha, D., Pottier, E., Bhattacharya, A., and Frery, A. C. (2020). A polsar scattering power factorization framework and novel roll-invariant parameter-based unsupervised classification scheme using a geodesic distance. *IEEE Transactions on Geoscience and Remote Sensing*, 58(5):3509–3525.

[12] Ressel, R., Singha, S., Lehner, S., Rösel, A., and Spreen, G. (2016). nvestigation into different polarimetric features for sea ice classification using x-band synthetic aperture radar. *IEEE Journal of Selected Topics in Applied Earth Observations and Remote Sensing*, 9(7):3131–3143.

[13] Touzi, R. (2007). Target scattering decomposition in terms of roll-invariant target parameters. *IEEE Trans. Geosci. Remote Sens.*, 45(1):73–84.

[14] Wakabayashi, H., Matsuoka, T., Nakamura, K., and Nishio, F. (2004). Polarimetric characteristics of sea ice in the sea of okhotsk observed by airborne l-band sar. *IEEE Trans. Geosci. Remote Sens.*, 42(11):2412–2425.